

# Principal deuterium Hugoniot via Quantum Monte Carlo and $\Delta$ -learning

Giacomo Tenti,<sup>1,\*</sup> Andrea Tirelli,<sup>1,†</sup> Kousuke Nakano,<sup>1,2,‡</sup> Michele Casula,<sup>3</sup> and Sandro Sorella<sup>1,4</sup>

<sup>1</sup>*International School for Advanced Studies (SISSA), Via Bonomea 265, 34136 Trieste, Italy*

<sup>2</sup>*School of Information Science, JAIST, Asahidai 1-1, Nomi, Ishikawa 923-1292, Japan*

<sup>3</sup>*Institut de Minéralogie, de Physique des Matériaux et de Cosmochimie (IMPMC), Sorbonne Université, CNRS UMR 7590, MNHN, 4 Place Jussieu, 75252 Paris, France*

<sup>4</sup>*Computational Materials Science Research Team, RIKEN Center for Computational Science (R-CCS), Kobe, Hyogo 650-0047, Japan*

(Dated: January 10, 2023)

We present a study of the principal deuterium Hugoniot for pressures up to 150 GPa, using Machine Learning potentials (MLPs) trained with Quantum Monte Carlo (QMC) energies, forces and pressures. In particular, we adopted a recently proposed workflow based on the combination of Gaussian kernel regression and  $\Delta$ -learning. By fully taking advantage of this method, we explicitly considered finite-temperature electrons in the dynamics, whose effects are highly relevant for temperatures above 10 kK. The Hugoniot curve obtained by our MLPs shows an excellent agreement with the most recent experiments, with an accuracy comparable to the best DFT functionals. Our work demonstrates that QMC can be successfully combined with  $\Delta$ -learning to deploy reliable MLPs for complex extended systems across different thermodynamic conditions, by keeping the QMC precision at the computational cost of a mean-field calculation.

*Introduction* – The study of hydrogen under extreme conditions has been a very active topic in condensed matter physics. Hydrogen is the most abundant element in the universe and the accurate knowledge of its phase diagram at pressures of the order of hundreds of GPa is extremely important for a variety of applications, such as modelling the interior of stars and giant gas planets [1–3], the inertial-confinement fusion [4], and the high- $T_c$  hydrogen-based superconductors [5, 6]. Nevertheless, several properties of this system are still highly debated, even at the qualitative level [7–10].

One of the main reasons that hamper our full understanding of high-pressure hydrogen is the difficulty of reproducing extreme pressures in a laboratory. Typical shock-wave experiments [11] make use of accelerated flyer plates to compress a material sample in a very short time, thus allowing to study the specimen at high temperatures and pressures. In particular, the set of possible end-states that the system can reach from some given initial conditions, also named *principal Hugoniot*, must satisfy a set of equations, known as Rankine-Hugoniot (RH) relations [12], linking the thermodynamic properties of the final shocked state with those of the starting one. During the years, the principal deuterium Hugoniot has been measured for a wide range of pressures and with a great degree of accuracy [13–20], reaching a relative error on the density as small as 2% in recent experiments.

In this context, numerical approaches, - in particular *Ab Initio* Molecular Dynamics (AIMD) simulations -, are extremely valuable, since they are not constrained by any experimental setup and can thus give further insight into this part of the phase diagram [21]. The Hugoniot region is particularly important because of the availability of experimental data that can be used to benchmark different theoretical methods. Among

them, Density Functional Theory (DFT) simulations have been extensively used and provided excellent results for the Hugoniot curve [22–28]. However, the approximations behind the particular exchange-correlation functional often produce discrepancies across existing DFT schemes whose accuracy varies according to the thermodynamic conditions, making the functional-based approach unsatisfactory. Quantum Monte Carlo (QMC) simulations, which depend on more controllable approximations, have also been performed [29, 30]. Although in principle more accurate and systematically improvable, these calculations have a much larger computational cost than DFT, and they are thus limited in system size and simulation length. Moreover, previous QMC calculations seem to give results for the principal Hugoniot in disagreement with the most recent experimental data, with the possible origin of this discrepancy being recently debated [31].

To overcome the large computational cost of *ab initio* simulations, machine learning techniques, aimed at constructing accurate potential energy surfaces, have become increasingly popular. Within this approach, one uses a dataset of configurations, i.e. the *training set*, to build a machine learning potential (MLP) that is able to reproduce energies and forces calculated with the given target method [32]. Unlike DFT MLPs, the QMC ones are relatively less common, given the larger computational cost and the consequent difficulty of generating large datasets, usually necessary to construct accurate MLPs.

In this work, we have successfully built a very accurate MLP with QMC energies, forces and pressures in the region of the deuterium Hugoniot, using the so-called  $\Delta$ -learning approach. The Hugoniot curve computed by the MLP shows an excellent agreement with the most recent

experiments, and it shares with the best DFT functionals the same, - if not better -, accuracy.

*Computational details* – In order to build an MLP with QMC references, we employed a combination of Gaussian Kernel Regression (GKR), Smooth Overlap of Atomic Positions (SOAP) descriptors [33], and  $\Delta$ -learning. The same approach has been recently proposed in Ref. 34, where it was applied to the study of high-pressure hydrogen in similar thermodynamic conditions. Following the  $\Delta$ -learning approach, an MLP is trained on the difference between the target method and a usually much cheaper *baseline* potential. Here, we trained 5 different MLPs, using Variational Monte Carlo (VMC) and Lattice Regularized Diffusion Monte Carlo (LRDMC) [35, 36] datapoints as targets, and several DFT baselines, with the Perdew-Zunger Local Density Approximation (PZ-LDA) [37], the Perdew-Burke-Ernzerhof (PBE) [38] and the van der Waals (vdW) -DF [39, 40] functionals. The QMC calculations were performed using the TURBORVB package [41].

To determine the principal Hugoniot, we made use of the RH jump equation:

$$H(\rho, T) = e(\rho, T) - e_0 + \frac{1}{2}(\rho^{-1} - \rho_0^{-1}) [p(\rho, T) + p_0] = 0, \quad (1)$$

where  $\rho$ ,  $T$ ,  $e(\rho, T)$ ,  $p(\rho, T)$  and  $\rho_0$ ,  $T_0$ ,  $e_0$ ,  $p_0$  are the density, temperature, energy per particle and pressure of the final and initial states, respectively. In particular, we ran a first set of  $NVT$  simulations at several temperatures in the [4 kK : 10 kK] range, and Wigner-Seitz radii between 1.80 Bohr and 2.28 Bohr, corresponding to the range where the zero of  $H(\rho, T)$  was expected. These simulations were performed considering classical nuclei and ground-state electrons, as quantum corrections and thermal effects have been shown to be negligible for these temperatures [30]. At each step, the energy, forces and pressure were calculated using the QUANTUM ESPRESSO package in its GPU accelerated version [42–44] with the chosen functional (PBE in most cases), and then corrected with our MLP trained on the difference between QMC and DFT data. The resulting dynamics has the same efficiency as a standard DFT AIMD simulation, which is roughly 100 times faster than the original QMC one. The details of our QMC simulations are reported in the Supplemental Material (SM) [45]. For the DFT simulations, we considered a 60 Ry plane-wave cutoff with a Projector Augmented Wave (PAW) pseudopotential [46] and a  $4 \times 4 \times 4$  Monkhorst-Pack  $k$ -point grid, while for the dynamics we used a time step of 0.25 fs and a Langevin thermostat [47, 48] with damping  $\gamma = 13 \text{ ps}^{-1}$ . For each temperature, the Hugoniot  $(\rho^*, p^*)$  coordinates are determined by fitting the Hugoniot function  $H(\rho, T)$  and the pressure  $p(\rho, T)$  with a spline function, and by numerically finding  $\rho^*$  and

the corresponding  $p^*$ .

Within our approach, we can fully take advantage of the  $\Delta$ -learning method by estimating the effect of thermalized electrons in our calculations. To do so, we considered two MLPs trained on the VMC-LDA and LRDMC-LDA differences, respectively, and ran simulations at temperatures  $T = 10 \text{ kK}$ ,  $15 \text{ kK}$ , and  $35 \text{ kK}$  with the corrected Karasiev-Sjostrom-Dufty-Trickey (KSDT) finite-temperature (FT) LDA functional [49–51] as baseline, in place of the usual ground-state PZ-LDA functional. In this way, we can include the effects of thermally excited electrons in our MLP without changing it, at least at the DFT level of theory.

*Results and Discussion* – Fig. 1a shows our results together with several experimental values for pressures below 150 GPa [16, 19, 20]. We also report the principal Hugoniot obtained by directly using the PBE baseline, and the Coupled Electron Ion Monte Carlo (CEIMC) results of Ref. 30 for comparison. For  $T = 10 \text{ kK}$  we show both the ground-state and FT results obtained with the procedure described previously, while for larger temperatures we plotted only the latter. Both the VMC and LRDMC models seem to reproduce very accurately the experimental points over the entire range of pressure considered. With respect to the most accurate data of Ref. 19, our estimate of the relative density  $\rho/\rho_0$  at the compressibility peak is only 1% lower for the VMC model and 3% lower for the LRDMC model, both being compatible within one error bar. Our results are in better agreement with experiments than the CEIMC ones reported in Ref. 30, which predicts a relative density 10% larger for the Hugoniot curve. The disagreement between the two results seems to be due to a large difference in the pressure estimates between the two methods, as further discussed in the SM [45].

Fig. 1b displays the same points in the  $u_p - U_s$  space, where  $u_p$  is the particle velocity and  $U_s$  is the shock velocity, the two being calculated using the following RH relations:

$$u_p = \sqrt{(p + p_0)(\rho_0^{-1} - \rho^{-1})},$$

$$U_s = \rho_0^{-1} \sqrt{\frac{p + p_0}{\rho_0^{-1} - \rho^{-1}}}.$$

The difference  $\Delta U_s$  between these points and the linear fit on the gas-gun data re-analyzed in Ref. 19 is also shown (bottom panel of Fig. 1b). Notice that the drop in the slope of  $U_s$  relative to  $u_p$  coincides with the onset of the molecular-atomic (MA) transition, while the magnitude of the  $\Delta U_s$  minimum relates to the position of the relative compression peak. In particular, the PBE Hugoniot curve manifests a premature start of the dissociation, while it predicts correctly the magnitude of the compressibility maximum. Remarkably, our QMC results are very similar to the experimental findings not

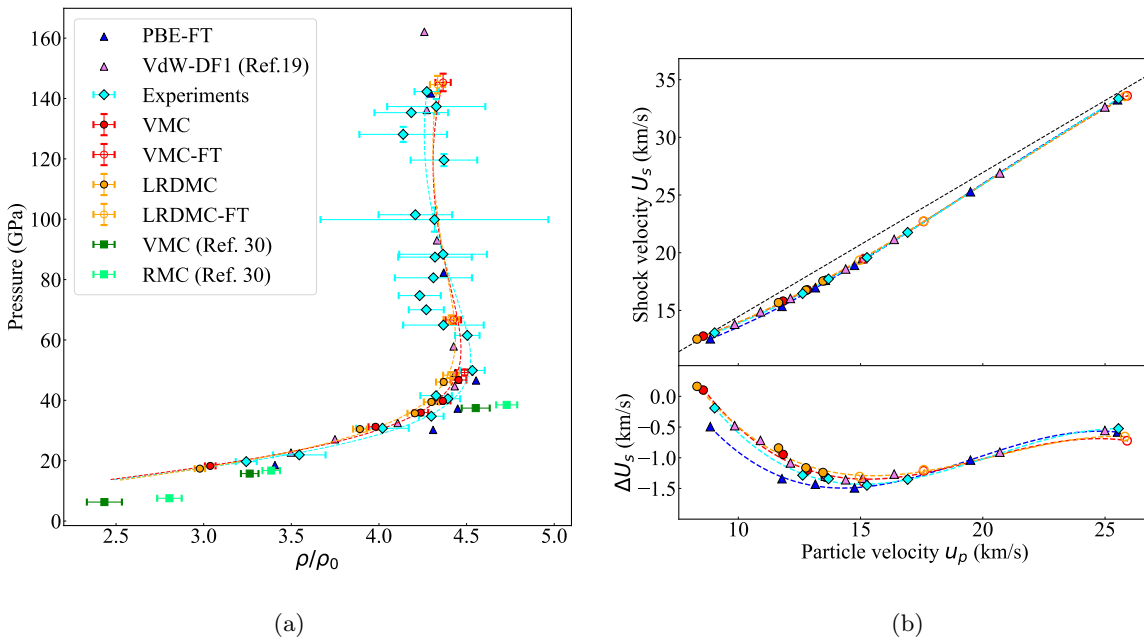


FIG. 1: **(1a)** Principal Hugoniot in the density-pressure space. Red and yellow circles are the results obtained with our MLPs trained on VMC and LRDMC datapoints, respectively, and a PBE baseline. Empty symbols refer to the results obtained using the finite-temperature (FT) KSDT functional as baseline. Blue and pink triangles are the PBE result calculated in this work and the VdW-DF1 result of Ref. 19 respectively. CEIMC results of Ref. 30 based on Variational Monte Carlo (VMC) and Reptation Monte Carlo (RMC) are reported in green squares. Cyan diamonds are the experimental results of Refs. 16, 19, and 20. Dashed-dotted lines are guides for the eye. **(1b)** [top panel] Hugoniot in the  $u_p$ - $U_s$  space. Black-dashed line is the re-analyzed gas-gun fit reported in Ref. 19. [bottom panel] Relative shock velocity with respect to the gas-gun fit. Only the experimental points of Ref. 19 are reported.

only for the compressibility peak but also for the shock velocity slope.

Thus, the Hugoniot curve obtained by our MLPs shows a much better agreement with the most recent experiments than the PBE functional, and is close to improved functionals, such as VdW-DF1 reported in Fig. 1, which has been proved more accurate than PBE for high pressure hydrogen [52]. Cancellation of errors taking place in the DFT Hugoniot [31] is less apparent in the  $\Delta U_s = \Delta U_s(u_p)$  relation (Fig. 1b), where the difference between PBE and improved theories is clear.

The presence of an MA transition is also investigated in Fig. 2, where we report the radial distribution function,  $g(r)$ , calculated on trajectories obtained with the LRDMC model for several temperatures at densities close to the Hugoniot curve. The inset of Fig. 2 displays the value of the molecular fraction  $m$ , defined as the percentage of atoms that stay within a distance of 2 Bohr (roughly corresponding to the first  $g(r)$  minimum after the molecular peak) from another particle for longer than a characteristic time, here set to 6 fs. The results show a distinct atomic character for  $T \geq 10$  kK and a clear molecular peak at lower temperatures.

*Error analysis* – To assess the quality of our principal Hugoniot determination, we analyzed the

possible sources of errors in relation to our machine learning scheme. There are three main sources of errors: the uncertainties in the fit of  $H(\rho, T)$ , the prediction error of the MLP, and the uncertainties in the reference state energy estimate, i.e.  $e_0$  in Eq. (1). We verified that, in our case, the error produced by the fit is negligible compared to the other two sources, which we will discuss next.

As mentioned before, we followed Ref. 34 to construct our MLPs and used a GKR model based on a modified version of the SOAP kernel [33]. Our final dataset, including both training and test sets, comprises 871 configurations selected through an iterative procedure with 128 hydrogen atoms each, where we calculated energies, pressures and forces at the VMC and LRDMC levels. These configurations correspond to temperatures from 4 kK up to 35 kK and Wigner-Seitz radii from 1.80 Bohr to 2.12 Bohr. Finite size corrections have also been estimated using the KZK functional [53].

Details on the training set construction and the QMC calculations, together with the performances of all MLP models can be found in the SM [45]. In particular we found a final root mean square error, calculated on the test set, of the order of 20 meV/atom for the energy, 130 meV/Å for the forces, and 0.1 GPa for the pressures.

At this point, it is worth to highlight some favourable

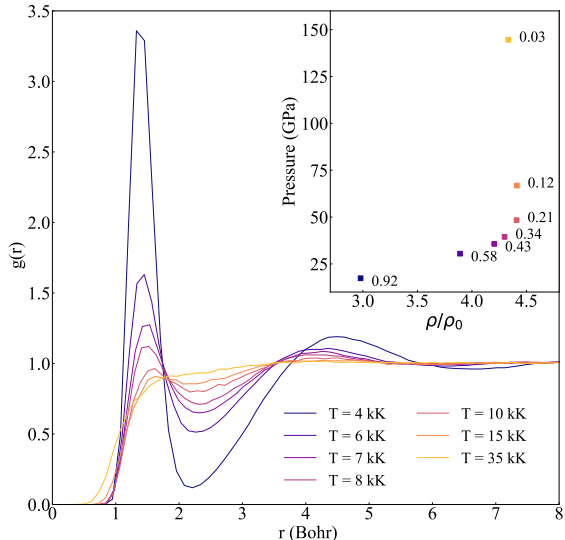


FIG. 2:  $g(r)$  for several temperatures and densities close to the principal Hugoniot, obtained using the LRDMC model. The molecular fraction value,  $m$ , is reported in the inset, beside each point distributed according to their corresponding location in the density-pressure space.

features of our machine learning approach, especially in applications where it is coupled with computationally expensive methods such as QMC. They can be itemized as follows:

- *transferability*: the total energy of the system is expressed as a sum of local terms [32], therefore our models are capable of making accurate predictions on configurations whose size has never been encountered in the training set. In particular, our MLPs find their applicability to systems with an arbitrary number of atoms  $N$ .
- *efficiency and accuracy*: within the  $\Delta$ -learning framework, the machine learning task becomes easier. Indeed, we obtained very accurate QMC potentials, by training models on small datasets and, thus, by reducing the amount of calculations needed. Moreover, since the computational cost of the ML inference is negligible compared to the baseline DFT calculation, we were able to perform QMC-driven MD simulations at the cost of a DFT dynamics.
- *overfitting prevention*: using a *local sparsification* technique based on the farthest point sampling (see SM of Ref. 34), we discarded from each configuration a possibly large fraction of the corresponding  $N$  local environments, preventing

overfitting and allowing for an increased predictive power of the model on unseen data. Since the computational cost of the predictions scales with the size of the training set, this procedure drastically improves the efficiency of the final model.

We further validated the accuracy of our MLP models by comparing the Hugoniot curve obtained using three potentials, independently trained with the same target, e.g. VMC, but with different baselines. In particular, we found the results to be consistent within an error of  $\lesssim 1\%$  and  $\lesssim 2\%$  for density and pressure, respectively.

We now turn to the last source of error we identified, i.e. the one related to the calculation of  $e_0$  and  $p_0$ . To estimate the reference state energy and pressure, we followed a procedure similar to Ref. 30. We performed a path integral molecular dynamics (PIMD) simulation [54] on a system of  $N = 64$  deuterium atoms at a temperature  $T = 22$  K and density  $\rho_0 = 0.167$  g/cm<sup>3</sup> (corresponding to the initial conditions reported in Ref. 19), using DFT-PBE energy and forces. Details of this simulation are reported in the SM [45]. From the PIMD trajectory, we extracted 170 configurations and we calculated energies and pressures with both DFT-PBE and QMC at VMC and LRDMC levels, adding the necessary finite size corrections. The reference sample was generated by extracting atomic positions from one of the 128 beads taken at random, belonging to de-correlated snapshots of the trajectory. Results for  $e_0$  for the various methods are reported in Tab. I. The reference state pressure  $p_0$  is not reported, since it is two orders of magnitude smaller than the shocked pressure, and thus irrelevant for the Hugoniot determination. Also in this case, we studied the effect of varying  $e_0$  within its confidence interval on the Hugoniot density and pressure. Its variability within standard deviation leads to shifts in the final principal Hugoniot which fall in the stochastic error range of our predictions.

To summarize, we estimated the MLP prediction error to be the most relevant source of uncertainty for the Hugoniot, yielding, as discussed before, an error of 1% and 2% on the relative density and pressure, respectively, reflected on the error bars reported in Fig. 1. Notice that our Hugoniot curve is consistent with the experiments even after considering the possible uncertainties.

	$e_{\text{pot}}$ (Ha/atom)	$e_0$ (Ha/atom)
PBE	-0.58217(2)	-0.58055(2)
VMC	-0.58465(3)	-0.58303(3)
LRDMC	-0.58653(2)	-0.58491(2)

TABLE I: Estimated potential ( $e_{\text{pot}}$ ) and total ( $e_0$ ) energies per atom of the reference state at  $\rho_0 = 0.167$  g/cm<sup>3</sup> and  $T = 22$  K for different methods.

*Conclusions* – In conclusion, using our recently proposed workflow for the construction of MLPs, we have been able to run reliable VMC- and LRDMC-based MD simulations and study the principal deuterium Hugoniot, in a pressure range relevant for experiments. The accuracy of the MLPs employed here has been extensively tested, supporting the validity of our calculations. The resulting Hugoniot curve shows an excellent agreement with the most recent measures, comparable to the best DFT functionals and better than previous QMC results. Moreover, within the  $\Delta$ -learning framework, we have also been able to treat FT electrons effects in a QMC-MLP, and we have thus managed to perform accurate simulations at higher temperatures. The efficiency of this approach could be further improved, e.g., by using cheaper baseline potentials than DFT. Longer simulations and larger systems will then be at reach. Other many-body methods, even more expensive than QMC, can also be used as targets for this type of MLPs, since the required size of the dataset is at least one order of magnitude smaller compared to other ML approaches. Finally, our MLPs, and in particular those trained on LRDMC datapoints, are promising for exploring the hydrogen phase diagram by keeping a high level of accuracy across a wide range of thermodynamic conditions.

*Data availability* – The machine learning code used in this work is available upon request. Additional information, such as datasets and detailed results of the simulations are available at [https://github.com/giacomotenti/QMC\\_hugoniot](https://github.com/giacomotenti/QMC_hugoniot).

*Acknowledgments.* The computations in this work have mainly been performed using the Fugaku supercomputer provided by RIKEN through the HPCI System Research Project (Project ID: hp210038 and hp220060) and Marconi100 provided by CINECA through the ISCRA project No. HP10BGJH1X and the SISSA three-year agreement 2022. K.N. is also grateful for computational resources from the facilities of Research Center for Advanced Computing Infrastructure at Japan Advanced Institute of Science and Technology (JAIST).

A.T. acknowledges financial support from the MIUR Progetti di Ricerca di Rilevante Interesse Nazionale (PRIN) Bando 2017 - grant 2017BZPKSZ. K.N. acknowledges a support from the JSPS Overseas Research Fellowships, that from Grant-in-Aid for Early-Career Scientists Grant Number JP21K17752, and that from Grant-in-Aid for Scientific Research(C) Grant Number JP21K03400. This work is supported by the European Centre of Excellence in Exascale Computing TREX - Targeting Real Chemical Accuracy at the Exascale. This project has received funding from the European Union's Horizon 2020 - Research and Innovation program - under grant agreement no. 952165. We dedicate this paper to the memory of Prof. Sandro

Sorella (SISSA), who tragically passed away during this project, remembering him as one of the most influential contributors to the quantum Monte Carlo community, and in particular for deeply inspiring this work with the development of the *ab initio* QMC code, TURBORVB.

---

\* [gtenti@sissa.it](mailto:gtenti@sissa.it)

† [atirelli@sissa.it](mailto:atirelli@sissa.it)

‡ [kousuke.1123@icloud.com](mailto:kousuke.1123@icloud.com)

- [1] D. Saumon, G. Chabrier, and H. M. van Horn, *The astrophysical journal supplement series* **99**, 713 (1995).
- [2] J. J. Fortney and N. Nettelmann, *Space Science Reviews* **152**, 423 (2009).
- [3] Y. Miguel, T. Guillot, and L. Fayon, *Astronomy & Astrophysics* **596**, A114 (2016).
- [4] S. Hu, V. Goncharov, T. Boehly, R. McCrory, S. Skupsky, L. A. Collins, J. D. Kress, and B. Militzer, *Physics of Plasmas* **22**, 056304 (2015).
- [5] A. P. Drozdov, M. I. Erements, I. A. Troyan, V. Ksenofontov, and S. I. Shylin, *Nature* **525**, 73 (2015).
- [6] M. Somayazulu, M. Ahart, A. K. Mishra, Z. M. Geballe, M. Baldini, Y. Meng, V. V. Struzhkin, and R. J. Hemley, *Phys. Rev. Lett.* **122**, 027001 (2019).
- [7] J. M. McMahon, M. A. Morales, C. Pierleoni, and D. M. Ceperley, *Rev. Mod. Phys.* **84**, 1607 (2012).
- [8] B. Cheng, G. Mazzola, C. J. Pickard, and M. Ceriotti, *Nature* **585**, 217 (2020).
- [9] V. V. Karasiev, J. Hinz, S. X. Hu, and S. B. Trickey, *Nature* **600**, E12 (2021).
- [10] B. Cheng, G. Mazzola, C. J. Pickard, and M. Ceriotti, *Nature* **600**, E15 (2021).
- [11] W. J. Nellis, *Reports on Progress in Physics* **69**, 1479 (2006).
- [12] G. E. Duvall and R. A. Graham, *Rev. Mod. Phys.* **49**, 523 (1977).
- [13] W. J. Nellis, A. C. Mitchell, M. van Thiel, G. J. Devine, R. J. Trainor, and N. Brown, *The Journal of Chemical Physics* **79**, 1480 (1983), <https://doi.org/10.1063/1.445938>.
- [14] M. D. Knudson, D. L. Hanson, J. E. Bailey, C. A. Hall, J. R. Asay, and W. W. Anderson, *Phys. Rev. Lett.* **87**, 225501 (2001).
- [15] G. V. Boriskov, A. I. Bykov, R. I. Il'kaev, V. D. Selemir, G. V. Simakov, R. F. Trunin, V. D. Urlin, A. N. Shuikin, and W. J. Nellis, *Phys. Rev. B* **71**, 092104 (2005).
- [16] M. D. Knudson, D. L. Hanson, J. E. Bailey, C. A. Hall, J. R. Asay, and C. Deeney, *Phys. Rev. B* **69**, 144209 (2004).
- [17] D. G. Hicks, T. R. Boehly, P. M. Celliers, J. H. Eggert, S. J. Moon, D. D. Meyerhofer, and G. W. Collins, *Phys. Rev. B* **79**, 014112 (2009).
- [18] P. Loubeyre, S. Brygoo, J. Eggert, P. M. Celliers, D. K. Spaulding, J. R. Rygg, T. R. Boehly, G. W. Collins, and R. Jeanloz, *Phys. Rev. B* **86**, 144115 (2012).
- [19] M. D. Knudson and M. P. Desjarlais, *Physical Review Letters* **118**, 1 (2017).
- [20] A. Fernandez-Pañella, M. Millot, D. E. Fratanduono, M. P. Desjarlais, S. Hamel, M. C. Marshall, D. J. Erskine, P. A. Sterne, S. Haan, T. R. Boehly, G. W. Collins, J. H.

- Eggert, and P. M. Celliers, *Phys. Rev. Lett.* **122**, 255702 (2019).
- [21] M. D. Knudson and M. P. Desjarlais, *Journal of Applied Physics* **129**, 10.1063/5.0050878 (2021).
- [22] T. J. Lenosky, S. R. Bickham, J. D. Kress, and L. A. Collins, *Phys. Rev. B* **61**, 1 (2000).
- [23] G. Galli, R. Q. Hood, A. U. Hazi, and F. m. c. Gygi, *Phys. Rev. B* **61**, 909 (2000).
- [24] S. Bagnier, P. Blottiau, and J. Cl  rouin, *Phys. Rev. E* **63**, 015301 (2000).
- [25] S. A. Bonev, B. Militzer, and G. Galli, *Phys. Rev. B* **69**, 014101 (2004).
- [26] B. Holst, R. Redmer, and M. P. Desjarlais, *Phys. Rev. B* **77**, 184201 (2008).
- [27] L. Caillabet, S. Mazevet, and P. Loubeyre, *Phys. Rev. B* **83**, 094101 (2011).
- [28] V. V. Karasiev, S. X. Hu, M. Zaghoo, and T. R. Boehly, *Physical Review B* **99**, 1 (2019).
- [29] N. M. Tubman, E. Liberatore, C. Pierleoni, M. Holzmann, and D. M. Ceperley, *Physical Review Letters* **115**, 1 (2015).
- [30] M. Ruggeri, M. Holzmann, D. M. Ceperley, and C. Pierleoni, *Physical Review B* **102**, 144108 (2020), [arXiv:2008.00269](https://arxiv.org/abs/2008.00269).
- [31] R. C. Clay, M. P. Desjarlais, and L. Shulenburger, *Physical Review B* **100**, 75103 (2019).
- [32] J. Behler and M. Parrinello, *Physical Review Letters* **98**, 1 (2007).
- [33] S. De, A. P. Bart  k, G. Cs  nyi, and M. Ceriotti, *Phys. Chem. Chem. Phys.* **18**, 13754 (2016).
- [34] A. Tirelli, G. Tenti, K. Nakano, and S. Sorella, *Phys. Rev. B* **106**, L041105 (2022).
- [35] M. Casula, C. Filippi, and S. Sorella, *Phys. Rev. Lett.* **95**, 100201 (2005).
- [36] K. Nakano, R. Maezono, and S. Sorella, *Phys. Rev. B* **101**, 155106 (2020).
- [37] J. P. Perdew and A. Zunger, *Phys. Rev. B* **23**, 5048 (1981).
- [38] J. P. Perdew, K. Burke, and M. Ernzerhof, *Phys. Rev. Lett.* **77**, 3865 (1996).
- [39] M. Dion, H. Rydberg, E. Schr  der, D. C. Langreth, and B. I. Lundqvist, *Phys. Rev. Lett.* **92**, 246401 (2004).
- [40] K. Berland, V. R. Cooper, K. Lee, E. Schr  der, T. Thonhauser, P. Hyldgaard, and B. I. Lundqvist, *Reports on Progress in Physics* **78**, 066501 (2015).
- [41] K. Nakano, C. Attacalite, M. Barborini, L. Capriotti, M. Casula, E. Coccia, M. Dagrada, C. Genovese, Y. Luo, G. Mazzola, A. Zen, and S. Sorella, *J. Chem. Phys.* **152**, 204121 (2020).
- [42] P. Giannozzi, S. Baroni, N. Bonini, M. Calandra, R. Car, C. Cavazzoni, D. Ceresoli, G. L. Chiarotti, M. Cococcioni, I. Dabo, A. D. Corso, S. de Gironcoli, S. Fabris, G. Fratesi, R. Gebauer, U. Gerstmann, C. Gougoussis, A. Kokalj, M. Lazzeri, L. Martin-Samos, N. Marzari, F. Mauri, R. Mazzarello, S. Paolini, A. Pasquarello, L. Paulatto, C. Sbraccia, S. Scandolo, G. Sclauzero, A. P. Seitsonen, A. Smogunov, P. Umari, and R. M. Wentzcovitch, *Journal of Physics: Condensed Matter* **21**, 395502 (2009).
- [43] P. Giannozzi, O. Andreussi, T. Brumme, O. Bunau, M. B. Nardelli, M. Calandra, R. Car, C. Cavazzoni, D. Ceresoli, M. Cococcioni, N. Colonna, I. Carnimeo, A. D. Corso, S. de Gironcoli, P. Delugas, R. A. DiStasio, A. Ferretti, A. Floris, G. Fratesi, G. Fugallo, R. Gebauer, U. Gerstmann, F. Giustino, T. Gorni, J. Jia, M. Kawamura, H.-Y. Ko, A. Kokalj, E. K    benli, M. Lazzeri, M. Marsili, N. Marzari, F. Mauri, N. L. Nguyen, H.-V. Nguyen, A. O. de-la Roza, L. Paulatto, S. Ponc  , D. Rocca, R. Sabatini, B. Santra, M. Schlipf, A. P. Seitsonen, A. Smogunov, I. Timrov, T. Thonhauser, P. Umari, N. Vast, X. Wu, and S. Baroni, *Journal of Physics: Condensed Matter* **29**, 465901 (2017).
- [44] P. Giannozzi, O. Baseggio, P. Bonf  , D. Brunato, R. Car, I. Carnimeo, C. Cavazzoni, S. de Gironcoli, P. Delugas, F. Ferrari Ruffino, A. Ferretti, N. Marzari, I. Timrov, A. Urru, and S. Baroni, *The Journal of Chemical Physics* **152**, 154105 (2020), <https://doi.org/10.1063/5.0005082>.
- [45] See Supplemental Material at [*URL will be inserted by publisher*] for additional information about the computational details of QMC calculations, the MLP training and validation, the reference state calculations, finite-size corrections, finite temperature DFT simulations, and comparison with previous results [28, 30, 34–36, 48–51, 53, 55–65].
- [46] H.PBEK-JPAW\_PSL.1.0.0.UPF pseudopotential available at [http://pseudopotentials.quantum-espresso.org/legacy\\_tables/ps-library/h](http://pseudopotentials.quantum-espresso.org/legacy_tables/ps-library/h).
- [47] A. Ricci and G. Ciccotti, *Molecular Physics - MOL PHYS* **101**, 1927 (2003).
- [48] C. Attacalite and S. Sorella, *Phys. Rev. Lett.* **100**, 114501 (2008).
- [49] V. V. Karasiev, T. Sjostrom, J. Dufty, and S. B. Trickey, *Phys. Rev. Lett.* **112**, 076403 (2014).
- [50] V. V. Karasiev, J. W. Dufty, and S. B. Trickey, *Phys. Rev. Lett.* **120**, 076401 (2018).
- [51] S. Lehtola, C. Steigemann, M. J. Oliveira, and M. A. Marques, *SoftwareX* **7**, 1 (2018).
- [52] R. C. Clay, J. Mcminis, J. M. McMahon, C. Pierleoni, D. M. Ceperley, and M. A. Morales, *Phys. Rev. B* **89**, 184106 (2014).
- [53] H. Kwee, S. Zhang, and H. Krakauer, *Phys. Rev. Lett.* **100**, 126404 (2008).
- [54] F. Mouhat, S. Sorella, R. Vuilleumier, A. M. Saitta, and M. Casula, *Journal of Chemical Theory and Computation* **13**, 2400 (2017).
- [55] M. Casula and S. Sorella, *J. Chem. Phys.* **119**, 6500 (2003).
- [56] S. Sorella, M. Casula, and D. Rocca, *J. Chem. Phys.* **127**, 014105 (2007).
- [57] K. Nakano, T. Morresi, M. Casula, R. Maezono, and S. Sorella, *Phys. Rev. B* **103**, L121110 (2021).
- [58] K. Nakano, A. Raghav, and S. Sorella, *The Journal of Chemical Physics* **156**, 034101 (2022).
- [59] C. J. Umrigar, *Int. J. Quantum Chem* **36**, 217 (1989).
- [60] S. Sorella and L. Capriotti, *J. Chem. Phys.* **133**, 234111 (2010).
- [61] C. Filippi, R. Assaraf, and S. Moroni, *J. Chem. Phys.* **144**, 194105 (2016).
- [62] J. van Rhijn, C. Filippi, S. De Palo, and S. Moroni, *Journal of chemical theory and computation* **18**, 118 (2021).
- [63] S. Pathak and L. K. Wagner, *AIP Adv.* **10**, 085213 (2020).
- [64] P. Reynolds, R. Barnett, B. Hammond, R. Grimes, and W. Lester Jr, *Int. J. Quantum Chem.* **29**, 589 (1986).
- [65] N. D. Mermin, *Phys. Rev.* **137**, A1441 (1965).

# Supplemental material: Principal deuterium Hugoniot via Quantum Monte Carlo and $\Delta$ -Learning

Giacomo Tenti\* and Andrea Tirelli<sup>†</sup>

*International School for Advanced Studies (SISSA),  
Via Bonomea 265, 34136 Trieste, Italy*

Kousuke Nakano<sup>‡</sup>

*International School for Advanced Studies (SISSA),  
Via Bonomea 265, 34136 Trieste, Italy and  
School of Information Science, JAIST,  
Asahidai 1-1, Nomi, Ishikawa 923-1292, Japan*

Michele Casula

*Institut de Minéralogie, de Physique des Matériaux et de Cosmochimie (IMPMC),  
Sorbonne Université, CNRS UMR 7590,  
MNHN, 4 Place Jussieu, 75252 Paris, France*

Sandro Sorella

*International School for Advanced Studies (SISSA),  
Via Bonomea 265, 34136 Trieste, Italy and  
Computational Materials Science Research Team,  
RIKEN Center for Computational Science (R-CCS), Kobe, Hyogo 650-0047, Japan*

(Dated: January 10, 2023)

## I. COMPUTATIONAL DETAILS OF QMC CALCULATIONS

The Variational Monte Carlo (VMC) and lattice regularized diffusion Monte Carlo (LRDMC) [1] calculations in this study were performed by TURBORVB package [2]. The package employs a many-body WF ansatz  $\Psi$  which can be written as the product of two terms, i.e.,  $\Psi = \Phi_{\text{AS}} \times \exp J$ , where the term  $\exp J$  and  $\Phi_{\text{AS}}$  are conventionally called Jastrow and antisymmetric parts, respectively. The antisymmetric part is denoted as the Antisymmetrized Geminal Power (AGP) that reads:  $\Psi_{\text{AGP}}(\mathbf{r}_1, \dots, \mathbf{r}_N) = \hat{A} \left[ \Phi(\mathbf{r}_1^\uparrow, \mathbf{r}_1^\downarrow) \Phi(\mathbf{r}_2^\uparrow, \mathbf{r}_2^\downarrow) \cdots \Phi(\mathbf{r}_{N/2}^\uparrow, \mathbf{r}_{N/2}^\downarrow) \right]$ , where  $\hat{A}$  is the antisymmetrization operator, and  $\Phi(\mathbf{r}^\uparrow, \mathbf{r}^\downarrow)$  is called the pairing function [3]. The spatial part of the geminal function is expanded over the Gaussian-type atomic orbitals:  $\Phi_{\text{AGP}}(\mathbf{r}_i, \mathbf{r}_j) = \sum_{l,m,a,b} f_{\{a,l\},\{b,m\}} \psi_{a,l}(\mathbf{r}_i) \psi_{b,m}(\mathbf{r}_j)$  where  $\psi_{a,l}$  and  $\psi_{b,m}$  are primitive Gaussian atomic orbitals, their indices  $l$  and  $m$  indicate different orbitals centered on atoms  $a$  and  $b$ , and  $i$  and  $j$  are coordinates of spin up and down electrons, respectively, and  $f_{\{a,l\},\{b,m\}}$  are the variational parameters. In this study, a basis set composed of [4s2p1d] Gaussian atomic orbitals (GTOs) was employed for the atomic orbitals of the antisymmetric part. The pairing function can be also written as  $\Phi_{\text{AGPn}}(\mathbf{r}_i, \mathbf{r}_j) = \sum_{k=1}^M \lambda_k \phi_k(\mathbf{r}_i) \phi_k(\mathbf{r}_j)$  with  $\lambda_k > 0$ , where  $\phi_k(\mathbf{r})$  is a molecular orbital, i.e.,  $\phi_k(\mathbf{r}) = \sum_{i=1}^L c_{i,k} \psi_i(\mathbf{r})$ . When the pairing function is expanded over  $M$  molecular orbitals where  $M$  is equal to half of the total number of electrons ( $N/2$ ), the AGP coincides with the Slater-Determinant ansatz. In this study, we restricted ourselves to a Jastrow-Slater determinant (JSD) by setting  $M = \frac{1}{2} \cdot N$ , wherein the coefficients of atomic orbitals, i.e.,  $c_{i,k}$ , were obtained by the build-in Density Functional theory (DFT) package (PREP), and were fixed during a VMC optimization.

The Jastrow term is composed of one-body, two-body and three/four-body factors ( $J = J_1 + J_2 + J_{3/4}$ ). The one-body and two-body factors are essentially used to fulfill the electron-ion and electron-electron cusp conditions, respectively, and the three/four-body factor is employed to consider further electron-electron correlations (e.g., electron-nucleus-electron). The one-body Jastrow is decomposed into the so-called homogeneous and inhomogeneous parts, i.e.,  $J_1 = J_1^{\text{hom}} + J_1^{\text{inh}}$ . The homogeneous one-body Jastrow factor is  $J_1^{\text{hom}}(\mathbf{r}_1, \dots, \mathbf{r}_N) = \sum_{i,l} \left( -(2Z_l)^{3/4} u(2Z_l^{1/4} |\mathbf{r}_i - \mathbf{R}_l|) \right)$  where  $\mathbf{r}_i$  are the electron positions,  $\mathbf{R}_l$  are the atomic positions with corresponding atomic number  $Z_l$ , and  $u(r)$  is a short-range function containing a variational parameter  $b$ :  $u(r) = \frac{b}{2} (1 - e^{-r/b})$ . The inhomogeneous one-body Jastrow factor  $J_1^{\text{inh}}$  is represented as:

\* gtenti@sissa.it

† atirelli@sissa.it

‡ knakano@sissa.it



$J_1^{\text{inh}}(\mathbf{r}_1, \dots, \mathbf{r}_N) = \sum_{i=1}^N \sum_{a=1}^{N_{\text{atom}}} \left( \sum_l M_{a,l} \chi_{a,l}(\mathbf{r}_i) \right)$ , where  $\mathbf{r}_i$  are the electron positions,  $\mathbf{R}_a$  are the atomic positions with corresponding atomic number  $Z_a$ ,  $l$  runs over atomic orbitals  $\chi_{a,l}$  (e.g., GTO) centered on the atom  $a$ ,  $N_{\text{atom}}$  is the total number of atoms in a system, and  $\{M_{a,l}\}$  are variational parameters. The two-body Jastrow factor is defined as:  $J_2(\mathbf{r}_1, \dots, \mathbf{r}_N) = \exp\left(\sum_{i<j} v(|\mathbf{r}_i - \mathbf{r}_j|)\right)$ , where  $v(r) = \frac{1}{2}r \cdot (1 - F \cdot r)^{-1}$  and  $F$  is a variational parameter. The three-body Jastrow factor is:  $J_{3/4}(\mathbf{r}_1, \dots, \mathbf{r}_N) = \exp\left(\sum_{i<j} \Phi_{\text{Jas}}(\mathbf{r}_i, \mathbf{r}_j)\right)$ , and  $\Phi_{\text{Jas}}(\mathbf{r}_i, \mathbf{r}_j) = \sum_{l,m,a,b} g_{a,l,m,b} \chi_{a,l}^{\text{Jas}}(\mathbf{r}_i) \chi_{b,m}^{\text{Jas}}(\mathbf{r}_j)$ , where the indices  $l$  and  $m$  again indicate different orbitals centered on corresponding atoms  $a$  and  $b$ . In this study, the coefficients of the three/four-body Jastrow factor were set to zero for  $a \neq b$  because it significantly decreases the number of variational parameters while rarely affects variational energies. A basis set composed of [3s] GTOs was employed for the atomic orbitals of the Jastrow part. The variational parameters in the Jastrow factor were optimized by the so-called stochastic reconfiguration [4] implemented in TURBORVB. Total energies and forces are calculated at the VMC and the LRDMC levels with the optimized wavefunctions. The LRDMC calculations were performed by the original single-grid scheme [1] with the discretization grid size  $a = 0.20$  Bohr. To alleviate the one-body finite-size effects, we have used twisted average boundary conditions (TABC) with a  $4 \times 4 \times 4$  Monkhorst-Pack grid.

To obtain a statistically meaningful value of VMC and LRDMC forces with finite variance [5], the so-called reweighting techniques are needed because the Hellmann–Feynman (HF) and Pulay terms may diverge when the minimum electron–nucleus distance vanishes and when an electronic configuration is close to the nodal surface, respectively [6]. The infinite variance of the first term is cured by applying the so-called space-warp coordinate transformation (SWCT) algorithm [6–9], whereas that of the second term can be alleviated by modifying the VMC sampling distribution using a modified trial wave function that differs from the original trial wave function only in the vicinity of the nodal surface [10], which we dub the Attaccalite and Sorella (AS) regularization. The AS regularization is not an optimal regularization for this purpose because it enforces a finite density of walkers on the nodal surface [11]. Therefore, in this study, we employed the regularization technique recently proposed by Pathak and Wagner [12] combined with mixed-averaged forces proposed by Reynolds [13].

## II. MLP TRAINING AND VALIDATION

### A. Dataset construction

To construct our dataset, we performed a first set of PBE MD simulations on a system of  $N = 128$  atoms for temperatures in the range [4kK, 20kK] and densities in the range [1.80 Bohr, 2.20 Bohr], from which we extracted 500 decorrelated snapshots. We then added other configurations according to an active learning scheme: with a model trained using this first dataset we ran MD simulations and iteratively selected new points where the MLP performances were expected to be poor. In particular we did this by monitoring, for each unseen configuration, the quantity

$$\chi = \frac{1}{N} \sum_{i=1}^N \min_{\mu \in \text{training set}} K(R_i, R_\mu) \quad (1)$$

where  $K(R_i, R_\mu)$  is the normalized SOAP kernel between the  $i$ -th local environment of the configuration  $R_i$  and the  $\mu$ -th local environment in the training set  $R_\mu$ . The number  $\chi$  defined in (1) gives a quantitative measure of "how far" the unknown configuration is from what is already included in the training set. At the end the final dataset, i.e., the one for which  $\chi$  did not drop under a certain fixed threshold (0.80 in our case) during the dynamics, comprised 871 configurations of 128 atoms in total. The final range of temperatures and Wigner-Seitz radii spanned by these configurations was [4 kK : 35 kK ] and [1.80 Bohr : 2.12 Bohr ], respectively.

### B. Training details

For the training procedure we followed the strategy outlined in [14, §I.B]: the cost function  $C$  employed is the regularised weighted sum of the RMSE on the observables, *i.e.*

$$C = C(c_\mu) = \alpha \text{MSE}(E, \hat{E}(c_\mu)) + \beta \text{MSE}(F, \hat{F}(c_\mu)) + \gamma \text{MSE}(P, \hat{P}(c_\mu)) + \lambda \|c_\mu\|^2,$$

where  $E, F, P$  are the vectors representing the observables obtained through QMC simulations and  $\hat{E}, \hat{F}, \hat{P}$  are the observables computed through GKR. For the choice of the model hyperparameters, a cross-validation test led the following:

- the cutoff radius used to compute local environments has been set to  $r_c = 5.0$  Bohr.
- the parameters  $\alpha, \beta, \gamma$  and  $\lambda$  determining the cost function  $C(c_\mu)$  have been set to  $10^{-1}, 1, 10^2$  and  $10^{-5}$  respectively.

### C. Models performance

The performances of the models employed are measured through the root mean squared error (RMSE) on the observables on which the models were trained. Such RMSEs are reported in Table I.

### D. Effect of different baselines

In order to further validate the accuracy of a MLP, a common strategy is to compare the results of the dynamics obtained using the trained model with those obtained with the target ab initio method directly, at least for some small system sizes. In our case this is not an easy task, given the large computational time that would be needed for computing energies and forces at each step with QMC. An alternative way to establish the performances of the models is to look at the variance of the results obtained with MLPs trained using different baselines. The Hugoniot function  $H(\rho, T)$  and pressure at  $T = 8$  kK are shown in Fig.(1).

We can estimate the error produced by using different baselines as 1% in the Hugoniot density and 1 – 2% ( $\lesssim 1GPa$ ) in the Hugoniot pressure.

## III. REFERENCE STATE CALCULATIONS

As explained in the main text, a crucial part in the numerical determination of the Hugoniot is to estimate the reference state energy per atom  $e_0$  and pressure  $p_0$ . In particular, having a precise

	$N_{conf}$	$N_{envs}$	RMSE $_E$ (Ha / atom)	RMSE $_f$ (Ha / Bohr)	RMSE $_p$ (a.u.)	RMSE $_p$ (GPa)
VMC - PBE	666	4965	$8.34 \times 10^{-4}$	$2.396 \times 10^{-3}$	$2.09 \times 10^{-6}$	0.061
VMC - LDA	778	4966	$8.25 \times 10^{-4}$	$3.358 \times 10^{-3}$	$2.48 \times 10^{-6}$	0.073
VMC - DF1	785	4961	$7.20 \times 10^{-4}$	$2.215 \times 10^{-3}$	$1.63 \times 10^{-6}$	0.048
LRDMC - PBE	666	4965	$7.28 \times 10^{-4}$	$2.507 \times 10^{-3}$	$3.36 \times 10^{-6}$	0.098
LRDMC - LDA	666	4965	$8.44 \times 10^{-4}$	$3.374 \times 10^{-3}$	$3.64 \times 10^{-6}$	0.11

TABLE I: Training set size and value of the RMSE on different observables as calculated on the test set for the final models used in the simulations.

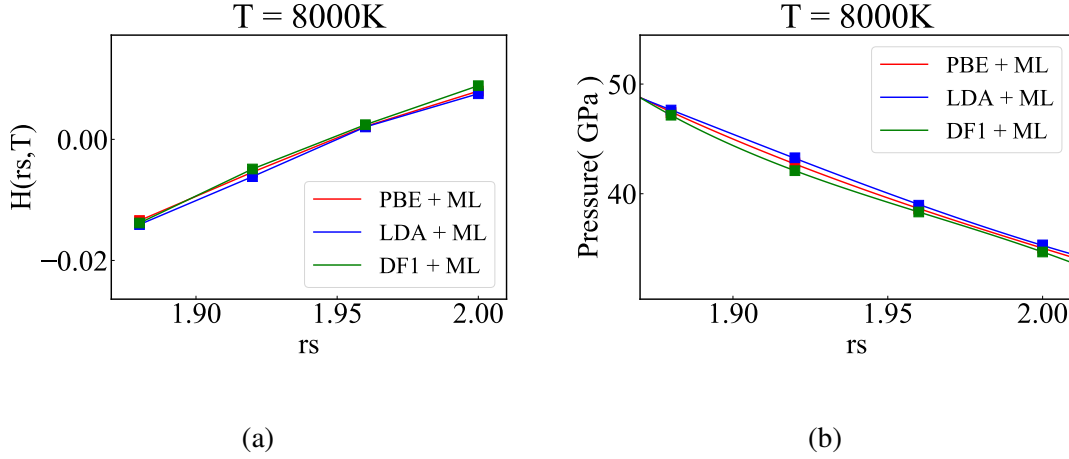


FIG. 1: Results for the Hugoniot function  $H(r_s, T)$  for  $T = 8$  kK with different MLPs trained on VMC data, using different baselines potentials.

value of  $e_0$  within the target method is important to take advantage of possible error cancellation effects and remove biases related to finite basis sets. We considered a system of  $N = 64$  deuterium atoms at  $T_0 = 22$ K and  $\rho_0 = 0.167$ g/cm<sup>-3</sup> and ran a path integral Ornstein-Uhlenbeck molecular dynamics [15] (PIOUMD) simulation to account for quantum effects, which are required because of the light deuterium mass and low temperature. Forces and energy were calculated with Density functional theory (DFT) through the Quantum-Espresso package. We checked the dependence of thermodynamic quantities on the number of replicas (or *beads*)  $M$  and on the choice of the DFT functional by studying the quantum kinetic energy  $T$  for several values of  $M$  using the BLYP and PBE functionals. In particular we considered two estimators for  $T$ , namely the virial and primitive (or Barker) estimator, given respectively by

$$T_{M, vir} = \frac{N}{2\beta} + \frac{1}{2M} \sum_{i=1}^{3N} \sum_{j=1}^M (x_i^{(j)} - \bar{x}_i) \partial_{x_i^{(j)}} V \quad (2)$$

$$T_{M, pri} = \frac{3NM}{2\beta} - \frac{mM}{2\beta^2 \hbar^2} \sum_{j=1}^M (x_i^{(j)} - x_i^{(j-1)})^2 \quad (3)$$

where  $M$  is the number of replicas used in the PIOUMD simulation,  $\mathbf{x}^{(j)} = (x_1^{(j)}, \dots, x_{3N}^{(j)})$  are the coordinates of the system belonging to the  $j$ -th bead,  $\bar{\mathbf{x}}_i = \frac{1}{M} \sum_{j=1}^M \mathbf{x}_i^{(j)}$  is the centroid position and  $\beta = k_B T_0$ . The results are shown in Fig.(2).

We noticed that a very large number of replicas is necessary for having a sufficiently converged result, while the value obtained with the two functionals is extremely similar for all values of  $M$ .

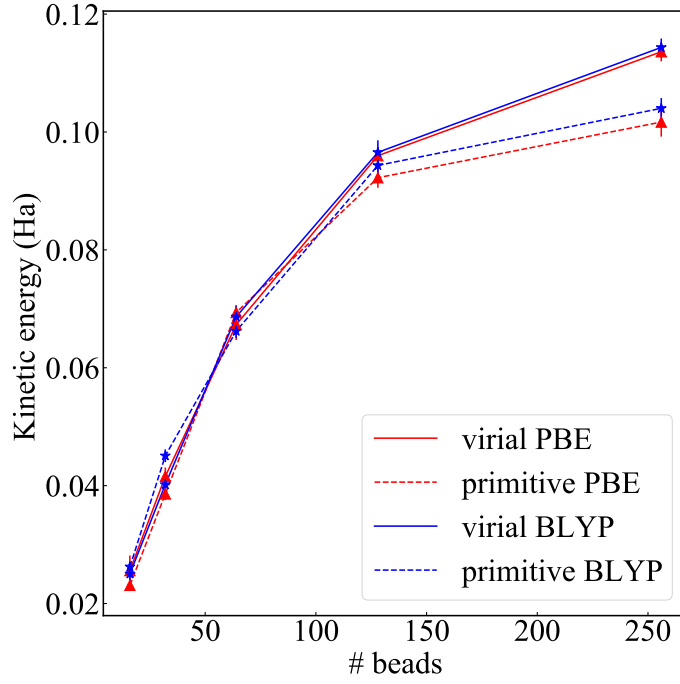


FIG. 2: Convergence of virial and primitive estimators for the quantum kinetic energy, as computed with Eqs. (2) (3), with the number of replica used in the PIMD simulation.

At the end we chose to use the PBE functional and  $M = 128$  replicas to have a reasonable trade-off between convergence and computational cost. For the DFT calculation we used a 60 Ry plane waves cutoff and a  $2 \times 2 \times 2$  Monkhorst-Pack  $k$  point mesh; for the dynamics we used a time step of 0.3 fs and let the system thermalize for 0.3 ps. We then extracted one configuration from a randomly chosen bead every 10 MD steps, for a total of  $N_{sample} = 170$  snapshots. Finally the potential energy of these configurations was calculated using the appropriate method (PBE, VMC or LRDMC). We then estimated  $e_0$  for each method as

$$e_0 = \frac{1}{N} \left( \frac{1}{N_{sample}} \sum_{sample} E_{pot}(\mathbf{x}_i) + T_{256, pri}^{PBE} \right) \quad (4)$$

using the value of the primitive estimator at  $M = 256$  beads as the best guess for the converged value of the kinetic energy. The approximation for the potential energy was checked by running PBE simulations on this set and confirming that the "true" mean value (as calculated by averaging over the beads and the trajectory) was consistent with our estimate obtained by averaging over the sample.

#### IV. FINITE SIZE CORRECTIONS

In this section we investigate the effect of finite size corrections (as estimated using the KZK functional [16]) on our results. In Fig.(3) we show the Hugoniot function ( at  $T = 4$  kK and  $T = 8$  kK) given by two models trained on VMC and VMC with finite size corrections respectively, both with a PBE baseline potential. The difference between the two turns out to be similar to the prediction error evaluated in Sec. II D, for the system size used in the simulations (i.e.,  $N = 128$ ). At the end we chose to apply finite size correction only for the model trained with LRDMC data.

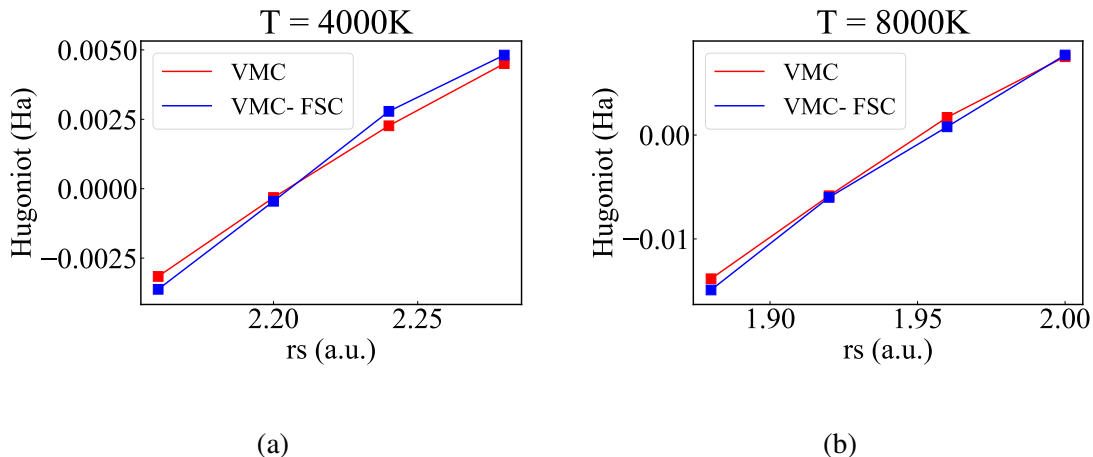


FIG. 3: Hugoniot function obtained using two MLPs trained on the difference between PBE and VMC with and without finite size corrections respectively, for  $T = 4$  kK and  $T = 8$  kK.

#### V. FINITE TEMPERATURE DFT SIMULATIONS

Using Mermin’s extension of the Hohenberg and Kohn theorems to non-zero temperature [17] we can treat finite temperature electrons in DFT by appropriately occupying the bands of the system according to the Fermi-Dirac distribution and minimizing the Helmholtz free energy functional  $A = E - TS$ . In this work we performed finite temperature DFT (FT-DFT) simulations to obtain the PBE Hugoniot and estimating the effect on the QMC Hugoniot. In the former case we used the zero temperature PBE functional for the simulations. Even if this is not rigorous, recent FT-DFT results on the Hugoniot using a temperature dependent GGA functional [18] have shown that for  $T \lesssim 40$  kK this approximation provides consistent results. For the latter application, we decided to use an explicitly temperature dependent functional to replace the LDA baseline of one

of the MLPs. In particular we used the corr-KSDT functional [19, 20], as implemented in the Libxc [21] library. This functional has the nice property to recover the standard PZ-LDA functional (that was used for the construction of the MLP under consideration) when  $T = 0K$ . In Fig. (4) we show the convergence of the free energy and some force components with the number of bands calculated for the KSDT functional at two values of temperature. In the simulations we decided to use 120 bands for  $T = 10$  kK and  $T = 15$  kK and 150 bands for  $T = 35$  kK.

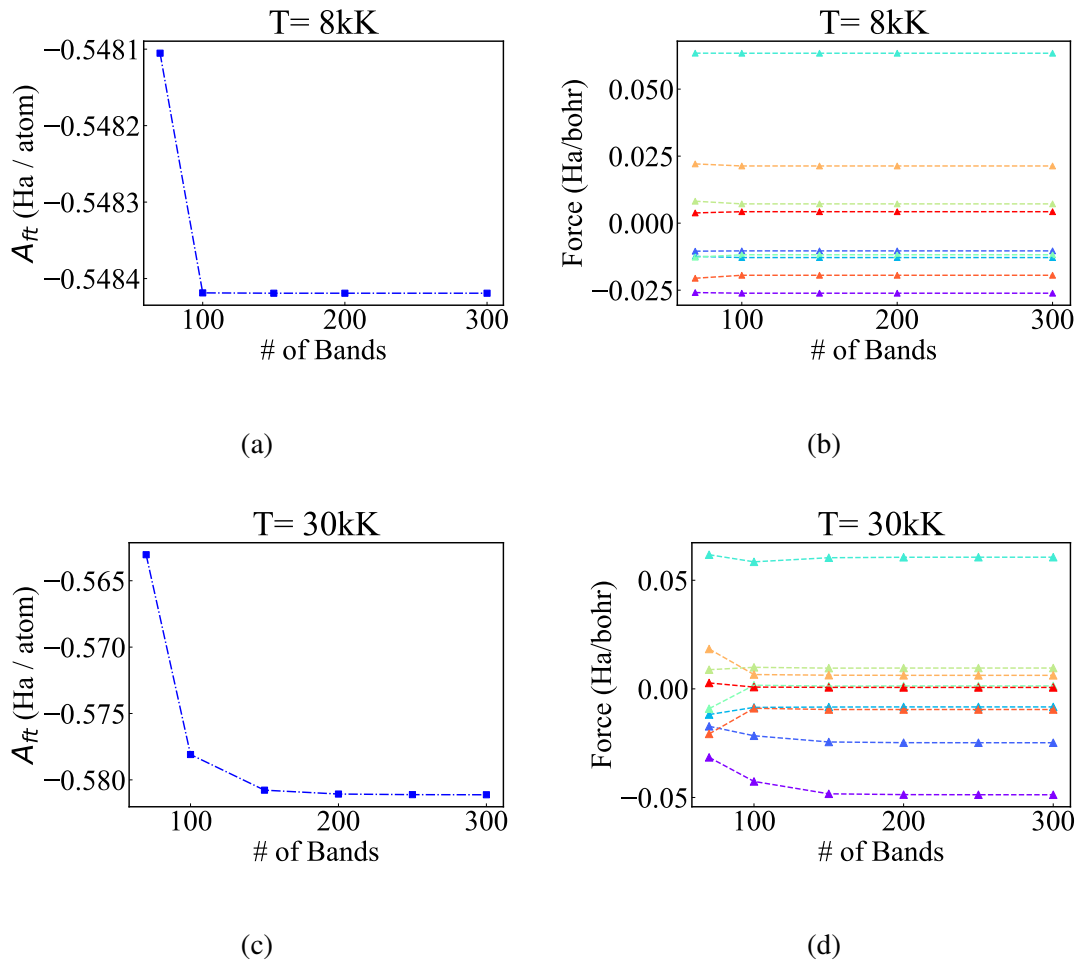


FIG. 4: Convergence of the free Energy  $A = E - TS$  and some forces components vs the number of bands calculated in the DFT for  $T = 8$  kK (4a, 4b) and  $T = 30$  kK (4c, 4d). Bands are occupied using the Fermi-Dirac distribution at the appropriate temperature.

## VI. COMPARISON WITH QMC CALCULATIONS OF REF. [22].

The equations of state at  $T = 8$  kK reported in Ref. [22] for both variational and reptation Monte Carlo are shown in Fig. (5), together with the VMC-MLP, LRDMC-MLP and the *ab initio* PBE ones. From this figure we can observe a huge discrepancy between the pressure estimated with our MLPs and the one in Ref. [22], which causes a sizable difference in the position of the Hugoniot. In our case the VMC and LRDMC pressures, which we then used for training, were calculated using the adjoint algorithmic differentiation method to obtain directly the derivative of the total energy with respect to the cell parameters. For LDA orbitals, as the ones used in this work, the pressure obtained with this procedure is not biased (see [14, §I.A]). Instead, in Ref. [22] a virial estimator was used, which can in principle produce discrepancies of the order of magnitude observed here, as shown in Ref. [23]. We also point out that the similarity between the LRDMC and VMC results suggests an overall robustness of our pressure estimation.

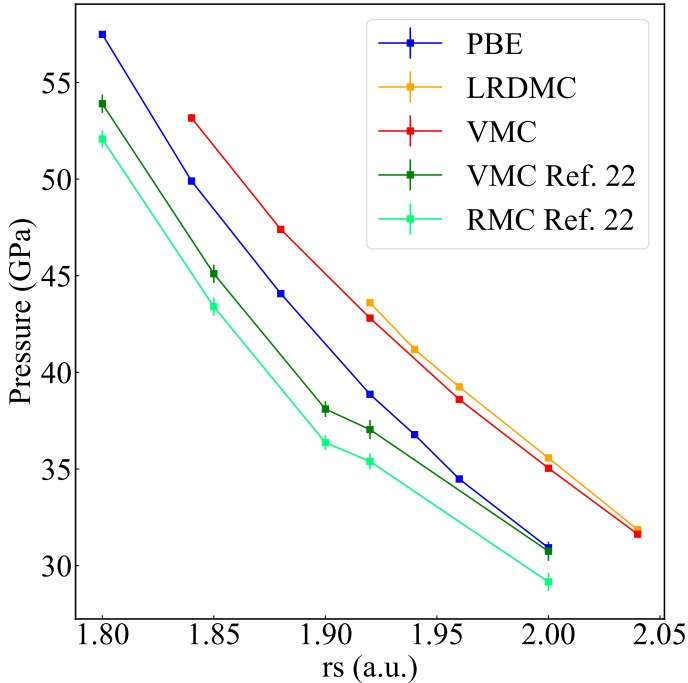


FIG. 5: Average pressure vs  $r_s$  for  $T = 8$  kK. Results obtained with our MLP are shown together with the ones reported in [22]



- 
- [1] M. Casula, C. Filippi, and S. Sorella, Diffusion monte carlo method with lattice regularization, *Phys. Rev. Lett.* **95**, 100201 (2005).
- [2] K. Nakano, C. Attaccalite, M. Barborini, L. Capriotti, M. Casula, E. Coccia, M. Dagrada, C. Genovese, Y. Luo, G. Mazzola, A. Zen, and S. Sorella, Turborvb: A many-body toolkit for ab initio electronic simulations by quantum monte carlo, *J. Chem. Phys.* **152**, 204121 (2020).
- [3] M. Casula and S. Sorella, Geminal wave functions with jastrow correlation: A first application to atoms, *J. Chem. Phys.* **119**, 6500 (2003).
- [4] S. Sorella, M. Casula, and D. Rocca, Weak binding between two aromatic rings: Feeling the van der waals attraction by quantum monte carlo methods, *J. Chem. Phys.* **127**, 014105 (2007).
- [5] K. Nakano, T. Morresi, M. Casula, R. Maezono, and S. Sorella, Atomic forces by quantum monte carlo: Application to phonon dispersion calculations, *Phys. Rev. B* **103**, L121110 (2021).
- [6] K. Nakano, A. Raghav, and S. Sorella, Space-warp coordinate transformation for efficient ionic force calculations in quantum monte carlo, *The Journal of Chemical Physics* **156**, 034101 (2022).
- [7] C. J. Umrigar, Two aspects of quantum monte carlo: determination of accurate wavefunctions and determination of potential energy surfaces of molecules, *Int. J. Quantum Chem* **36**, 217 (1989).
- [8] S. Sorella and L. Capriotti, Algorithmic differentiation and the calculation of forces by quantum monte carlo, *J. Chem. Phys.* **133**, 234111 (2010).
- [9] C. Filippi, R. Assaraf, and S. Moroni, Simple formalism for efficient derivatives and multi-determinant expansions in quantum monte carlo, *J. Chem. Phys.* **144**, 194105 (2016).
- [10] C. Attaccalite and S. Sorella, Stable liquid hydrogen at high pressure by a novel ab initio molecular-dynamics calculation, *Phys. Rev. Lett.* **100**, 114501 (2008).
- [11] J. van Rhijn, C. Filippi, S. De Palo, and S. Moroni, Energy derivatives in real-space diffusion monte carlo, *Journal of chemical theory and computation* **18**, 118 (2021).
- [12] S. Pathak and L. K. Wagner, A light weight regularization for wave function parameter gradients in quantum monte carlo, *AIP Adv.* **10**, 085213 (2020).
- [13] P. Reynolds, R. Barnett, B. Hammond, R. Grimes, and W. Lester Jr, Quantum chemistry by quantum monte carlo: Beyond ground-state energy calculations, *Int. J. Quantum Chem.* **29**, 589 (1986).
- [14] A. Tirelli, G. Tenti, K. Nakano, and S. Sorella, High-pressure hydrogen by machine learning and quantum monte carlo, *Phys. Rev. B* **106**, L041105 (2022).

- [15] F. Mouhat, S. Sorella, R. Vuilleumier, A. M. Saitta, and M. Casula, Fully quantum description of the zundel ion: Combining variational quantum monte carlo with path integral langevin dynamics, *Journal of Chemical Theory and Computation* **13**, 2400 (2017).
- [16] H. Kwee, S. Zhang, and H. Krakauer, Finite-size correction in many-body electronic structure calculations, *Phys. Rev. Lett.* **100**, 126404 (2008).
- [17] N. D. Mermin, Thermal properties of the inhomogeneous electron gas, *Phys. Rev.* **137**, A1441 (1965).
- [18] V. V. Karasiev, S. X. Hu, M. Zaghoo, and T. R. Boehly, Exchange-correlation thermal effects in shocked deuterium: Softening the principal Hugoniot and thermophysical properties, *Physical Review B* **99**, 1 (2019).
- [19] V. V. Karasiev, T. Sjoström, J. Dufty, and S. B. Trickey, Accurate homogeneous electron gas exchange-correlation free energy for local spin-density calculations, *Phys. Rev. Lett.* **112**, 076403 (2014).
- [20] V. V. Karasiev, J. W. Dufty, and S. B. Trickey, Nonempirical semilocal free-energy density functional for matter under extreme conditions, *Phys. Rev. Lett.* **120**, 076401 (2018).
- [21] S. Lehtola, C. Steigemann, M. J. Oliveira, and M. A. Marques, Recent developments in libxc — a comprehensive library of functionals for density functional theory, *SoftwareX* **7**, 1 (2018).
- [22] M. Ruggeri, M. Holzmann, D. M. Ceperley, and C. Pierleoni, Quantum Monte Carlo determination of the principal Hugoniot of deuterium, *Physical Review B* **102**, 144108 (2020), arXiv:2008.00269.
- [23] R. C. Clay, M. P. Desjarlais, and L. Shulenburger, Deuterium Hugoniot: Pitfalls of thermodynamic sampling beyond density functional theory, *Physical Review B* **100**, 75103 (2019).
- [24] K. Nakano, R. Maezono, and S. Sorella, Speeding up ab initio diffusion monte carlo simulations by a smart lattice regularization, *Phys. Rev. B* **101**, 155106 (2020).